Dalton Transactions

PAPER

View Article Online
View Journal

Cite this: DOI: 10.1039/c7dt00978j

Magnetic structure and properties of centrosymmetric twisted-melilite $K_2CoP_2O_7$†

Matthew Sale, [a,b] Maxim Avdeev, *[a,b] Zakiah Mohamed,[b] Chris D. Ling[b] and Prabeer Barpanda [c]

Received 17th March 2017,
Accepted 22nd April 2017

DOI: 10.1039/c7dt00978j

rsc.li/dalton

Twisted-melilite dipotassium cobalt pyrophosphate ($K_2CoP_2O_7$, $P4_2/mnm$, #136), originally reported by Gabelica-Robert (1981), was synthesized in powder form by a standard solid-state reaction route. The magnetic properties of the material were studied by magnetometry and its magnetic structure determined using neutron powder diffraction for the first time. Below T_N = 11 K, the material adopts a G-type antiferromagnetic structure with moments aligned in the *ab*-plane (magnetic space group *Pn'nm*, #58.3.473). *Ab initio* calculations were performed to examine the isotropic magnetic spin exchange parameters as well as the preferred direction of magnetic moments due to spin–orbit coupling. The relationship between crystal structure geometry and the strength of the magnetic interactions was examined and compared to those of melilite-type $Sr_2CoGe_2O_7$.

Introduction

Many oxides of the general formula $A_2BC_2O_7$ (where A = alkali, alkali-earth or rare-earth cations; larger B = Al, Be, Ga, Ge, Mg, Si, or transition metal; and smaller C = Al, Be, Ga, Ge, P, Si, V) adopt the melilite-type crystal structure.[1] This series is exemplified by the solid-solution between akermanite ($Ca_2MgSi_2O_7$) and gehlenite ($Ca_2Al_2SiO_7$).[2,3] The structure is built of layers of vertex-sharing BO_4 and CO_4 tetrahedra separated by alkali metal atoms A residing in the interlayer space (Fig. 1, left). It is described by a non-centrosymmetric tetragonal space group $P\bar{4}2_1m$ (#113) with unit cell parameters in the range $a = b \approx 7.3$–8.6 Å and $c \approx 4.8$–5.6 Å.[1] Many melilites form an incommensurate phase at lower temperatures due to a "misfit between the intermediate cation layer and the sheet-like tetrahedral framework".[1]

The melilite-type materials with transition metals have attracted substantial interest because the two-dimensional character of the magnetic sublattice leads to a variety of magnetic properties and structures, from incommensurate spiral to collinear Néel type, as summarized in Table 1. The primary magnetic interaction between B-site transition metal atoms in this class of materials is the intralayer super–super exchange (SSE) *via* –O–(C)–O– bond chains. Depending on the type of magnetic atom as well as the relative strength of different types of magnetic interactions, the melilite-type materials develop long-range commensurate, *e.g.* $Ba_2MnGe_2O_7$,[4] $Sr_2CoGe_2O_7$,[5] or incommensurate, *e.g.* $Ba_2CuGe_2O_7$ [6] magnetic order. However, the number of studied melilite-type magnetic systems remains rather small and further studies are needed in order to establish a connection between the composition and crystal structural parameters with the ground state magnetic structure type.

In order to better understand the relationship between the melilite crystal structural features and its magnetic properties, we have set out to explore the effect of mutual orientation of the transition metal layers. In this work, we focus on the magnetic structure and properties of $K_2CoP_2O_7$, which features tetrahedral layers identical to those of melilite but with every second layer rotated by 90° around the *c*-axis (Fig. 1, right). We will hereafter refer to this as the twisted-melilite structure. The rotation leaves the positions of interlayer A atoms virtually intact but changes their oxygen coordination from distorted square anti-prismatic to distorted square prismatic, doubling the *c*-axis, and creating an inversion center, with the resultant centrosymmetric space group $P4_2/mnm$ (#136). We note that while such a 90° rotation of half of the tetrahedral layers conveniently highlights the relationship between the two structure types, a real transformation of this type would require a high-energy reconstructive phase transition, no examples of which have been reported so far.

[a]*Australian Centre for Neutron Scattering, Australian Nuclear Science and Technology Organization, Locked Bag 2001, Kirrawee DC, NSW 2232, Australia. E-mail: max@ansto.gov.au*
[b]*School of Chemistry, The University of Sydney, Sydney, NSW 2006, Australia*
[c]*Faraday Materials Laboratory, Materials Research Center, Indian Institute of Science, C.V. Raman Avenue, Bangalore, 560012, India*
†Electronic supplementary information (ESI) available. See DOI: 10.1039/c7dt00978j

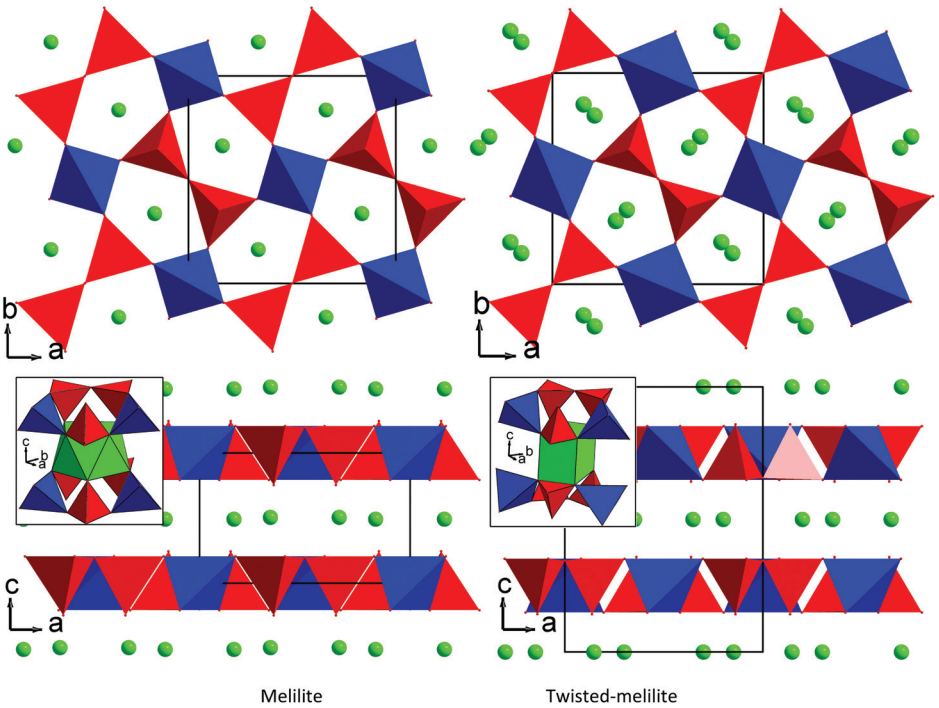

Fig. 1 View of the melilite-type structure ($Sr_2CoGe_2O_7$, $P\bar{4}2_1m$, left, ref. 5) and twisted-melilite type structure ($K_2CoP_2O_7$, $P4_2/mnm$, right). Blue and red tetrahedra and green balls show CoO_4 and BO_4 polyhedra and A cations, respectively. The view along the *c*-axis (top) shows that the tetrahedral layers in both structures are virtually identical. The view along the *b*-axis (bottom) illustrates that the tetrahedra in all the layers point in the same ($P\bar{4}2_1m$, left) and opposite direction ($P4_2/mnm$, right) for melilite and twisted-melilite, respectively. Anti-prismatic and prismatic coordination of A cations in the two structure types is shown in the insets.

Table 1 Magnetic properties of melilite and twisted-melilite compounds with Co as a B-site atom. The asterisk (*) indicates that exact space group was not determined and was inferred in this work based on the unit cell parameters and chemical formula

Composition	Space group	T_N (K)	θ (K)	Effective magnetic moment (μ_B)	Magnetic structure	Ref.
$Ca_2CoSi_2O_7$	$P\bar{4}2_1m$	5.6–5.7			AFM	30 and 31
$Sr_2CoSi_2O_7$	$P\bar{4}2_1m$	6.7			Canted AFM	30–32
$Ba_2CoSi_2O_7$	$P\bar{4}2_1m$					33
$K_2CoAs_2O_7$	$P4_2/mnm$*					8
$Sr_2CoGe_2O_7$	$P\bar{4}2_1m$	6.4–6.5	−18.1(6)	4.43(5)	C-Type AFM	5
$Ba_2CoGe_2O_7$	$P\bar{4}2_1m$	6.7	−33.4 ± 0.3 ∥ [001] −4.35 ± 1.1 ⊥ [001]	4.35 ∥ [001] 4.88 ⊥ [001]	Weakly canted C-Type AFM $J_1 = -2.3$ K, $J_2 = 0.2$ K	34–39
$Na_2CoP_2O_7$	$P4_2/mnm$	10	−19	4.40	AFM	8, 10 and 40
$K_2CoV_2O_7$	$P\bar{4}2_1m$	?	≈0	4.71	Paramagnet, 2–300 K	41
$K_2CoP_2O_7$	***$P4_2/mnm$***	**11**	**−22.5**	**4.63**	**G-Type AFM**	**8 and 11, this work**

The first members of the twisted-melilite type were reported by Majling ($Na_2ZnP_2O_7$)[7] and Gabelica-Robert (A = Na, K; C = P, As, V; B = Mg, Co, Cu, Zn).[8] However, only chemical formula, lattice parameters, and tetragonal lattice type were established. The first fully characterized twisted-melilite crystal structure was of $K_2MgV_2O_7$.[9]

The main motivation of this work was to investigate whether the changes in tetrahedral layer stacking and addition of an inversion center have any effect on the magnetic properties or magnetic structure of these melilite related compounds. While several melilite-type oxides were studied as magnetic systems, (ref. 5 and Table 1), to our knowledge, no magnetic structure has been reported for the twisted-melilite type materials; only magnetic property measurements were performed for $Na_2CoP_2O_7$.[10] The potassium analogue, $K_2CoP_2O_7$, was previously synthesized but only the twisted-melilite type of the crystal structure was reported based on powder and later single crystal X-ray diffraction.[8,11] Neither magnetic properties nor magnetic structure were studied. Here, we report the results of magnetometry, neutron powder diffraction and *ab initio* density functional theory (DFT) calculations for the centrosymmetric twisted-melilite type $P4_2/mnm$ $K_2CoP_2O_7$ pyrophosphate.

Materials, methods and calculations

Material synthesis

The royal blue colored powder sample of $K_2CoP_2O_7$ was synthesized by standard solid-state reaction from analytical grade KH_2PO_4 and CoC_2O_4 at 600 °C. An intimate stoichiometric 2 : 1 molar mixture of KH_2PO_4 (Sigma Aldrich, 99%) and CoC_2O_4 (SD Fine Chemicals, 97%) was prepared by wet planetary ball milling in acetone media for 1 h (600 rpm) using Cr-hardened stainless-steel (Cr-SS) milling media and container with the ratio of balls/precursor powder fixed at 10 : 1 (w/w). In a typical synthesis, 30 grams of spherical balls were used to mix 3 g of precursor mixture. Following, the acetone was dried, and the precursor mixture was ground, pressed into pellets, and sintered at 600 °C with a heating rate of 10 °C min^{-1} for 8 h in a tubular furnace under argon flow to obtain the desired phase.

X-ray diffraction analysis

X-ray powder diffraction patterns on $K_2CoP_2O_7$ were obtained with a Bruker AXS D8 ADVANCE diffractometer (operating at 35 mA, 40 kV) equipped with a Co K_α source (λ_1 = 1.78897 Å, λ_2 = 1.7929 Å) and a Vantec-1 linear position-sensitive detector.

DC magnetic susceptibility

DC magnetic susceptibility measurements were conducted with a Quantum Design PPMS instrument. Susceptibility was recorded in a zero-field cooled (ZFC) and field-cooled (FC) modes with an applied field of 10 kOe over the temperature range 2–300 K.

Neutron powder diffraction

Neutron powder diffraction (NPD) patterns were collected on the high-resolution powder diffractometer Echidna at the OPAL facility (Lucas Heights, Australia) using neutrons of wavelength 2.4395 Å. Approximately 4 g of powder sample were loaded in a 6 mm diameter cylindrical vanadium can, and diffraction patterns were collected between at 3 K and 20 K using a closed-cycle refrigerator. The magnetic structure was analyzed using the FullProf Suite[12] with the default neutron scattering lengths and Co^{2+} magnetic form factor.

Calculation details

In our DFT study of $K_2CoP_2O_7$, we used the Vienna *Ab initio* Simulation Package (VASP) (version 5.2.12)[13–16] in the generalized gradient approximation (GGA) of Perdew, Burke and Ernzerhof[17] with the projector augmented-wave (PAW) method.[18,19] A Γ-centered 2 × 2 × 1 Monkhorst–Pack *k*-point mesh[20] with the linear tetrahedron smearing method[21] was used for the calculations with a plane wave energy cut-off of 500 eV. The GGA + onsite repulsion (GGA + U) method was used to correct the well-known over-binding of electrons in the 3d metals.[22] No supercell was necessary as the experimental magnetic configuration was of the same dimensions as the chemical unit cell.

Results and discussion

X-ray powder diffraction

Based on the X-ray powder diffraction data, the sample was found to be practically phase pure with only a minor impurity of monoclinic KPO_3.[23] The fraction of KPO_3 was further determined in the course of NPD data analysis at the level of ~2 wt%. This non-magnetic impurity did not affect further magnetometry and magnetic structure NPD data analysis.

Magnetic susceptibility

The magnetic susceptibility as a function of temperature measured from 2–300 K showed magnetic ordering below the Néel ordering temperature of 11 K (Fig. 2). This Néel ordering temperature is very close to the 10 K value for isostructural $Na_2CoP_2O_7$, which has a different A-site interlayer cation (Table 1). Below this temperature, the material is antiferromagnetic, which is indicated by the decreasing magnetic susceptibility. No divergence of the FC and ZFC magnetic susceptibility curves was observed indicating the absence of a spin-glass state.

The ZFC magnetic susceptibility was fitted to the modified Curie–Weiss law $\chi_{exp} = C/(T - \theta) + \chi_{TIP}$ where C is the Curie constant, θ is the Curie–Weiss temperature, and χ_{TIP} is the temperature independent paramagnetic contribution. The results are illustrated in Fig. 2 and summarized in Table 1. This fit yielded a Curie–Weiss temperature of −22.5 K, which indicated predominantly antiferromagnetic interactions. The frustration index $|\theta_{CW}|/T_N \sim 2$ indicated the absence of substantial spin frustration in this material. This data also yielded an effective magnetic moment of 4.63μ_B, suggesting contribution from the partially unquenched orbital angular momentum, typical for Co^{2+}. These values are comparable to those for similar materials (Table 1). Measurements of the magnetic hysteresis below the Néel ordering temperature were also performed (Fig. 3) and linear response typical of an antiferromagnet was observed.

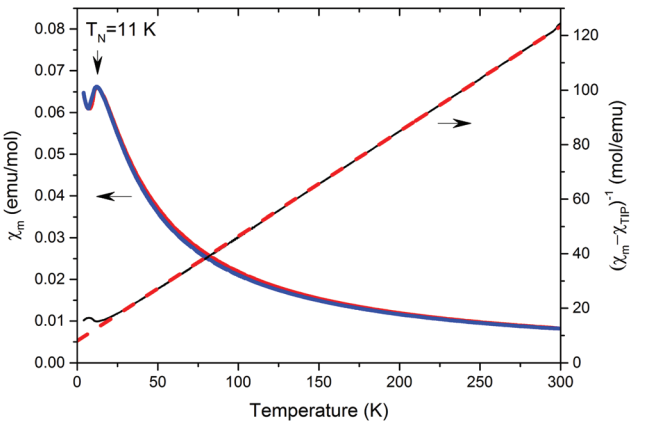

Fig. 2 ZFC (red) and FC (blue) DC magnetic susceptibility for $K_2CoP_2O_7$ from 2–300 K and inverse magnetic susceptibility with a fit of the ZFC data to the modified Curie–Weiss law.

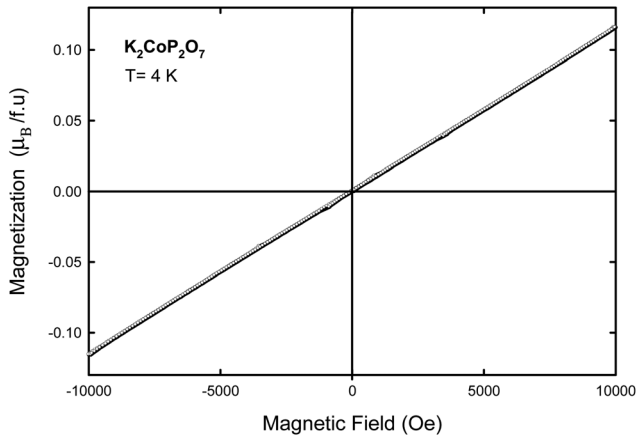

Fig. 3 Magnetization as a function of field for $K_2CoP_2O_7$ at 4 K showing no ferromagnetic signal.

Neutron powder diffraction

The crystal structure of $K_2CoP_2O_7$ was refined from neutron powder diffraction data (Fig. 4 and Table S1†) collected at 3 K and 20 K, *i.e.* below and above the magnetic ordering transition temperature. Refinement confirmed the centrosymmetric space group $P4_2/mnm$ (#136). This material has the unit cell length doubled in the *c* direction compared to the melilite family of materials due to the 90° rotation of every second $[CoP_2O_7]^{2-}$ layer.

The NPD pattern taken at 3 K, *i.e.* below the Néel temperature, showed the emergence of distinct peaks due to the ordering of the magnetic moments of Co. All the magnetic peaks could be indexed by the chemical unit cell, *i.e.* with the propagation vector k = (0,0,0). Representational analysis performed with BasIreps for the Co atoms located in the 4d(1/2,0,1/4) site (Table S6†) followed by model testing unambiguously pointed to the magnetic structure in which each Co is antiferromagnetically coupled to its six nearest neighbors, the so called G-type structure. Further comparison of the G-type models with the moments along the *c* and *a*/*b* axes, magnetic space groups $P4'_2/m'n'm$ (#136.6.1157) and $Pn'nm$ (#58.3.473), respectively, revealed that the latter provides better agreement with the experimental data, with magnetic *R*-factors of 5.53% and 4.43%, respectively. We note that the $Pn'nm$ magnetic space group (or irreducible representation #9 in the BasIreps notation) allows an additional moment component in the *ab* plane *via* contribution of basis vectors #2 or #4 (Table S6†), which, if present, would result in a non-collinear magnetic structure or, in the extreme case, collinear A-type magnetic structure. However, the experimental data showed no corresponding magnetic intensity. We therefore conclude that the magnetic structure of $K_2CoP_2O_7$ is of collinear G-type with the moment in the *ab*-plane, described by the $Pn'nm$ (#58.3.473) magnetic space group (Fig. 6b). It should be noted that powder diffraction cannot determine the direction of the collinear moments within the *ab*-plane, *i.e.* relative contribution of the basis vectors #1 and #3 (Table S6†), and therefore our choice of the moment direction along *a*-axis is arbitrary. The refined value of the magnetic moment, 3.03(3)μ_B, is very close to that expected for S = 3/2 Co^{2+}.

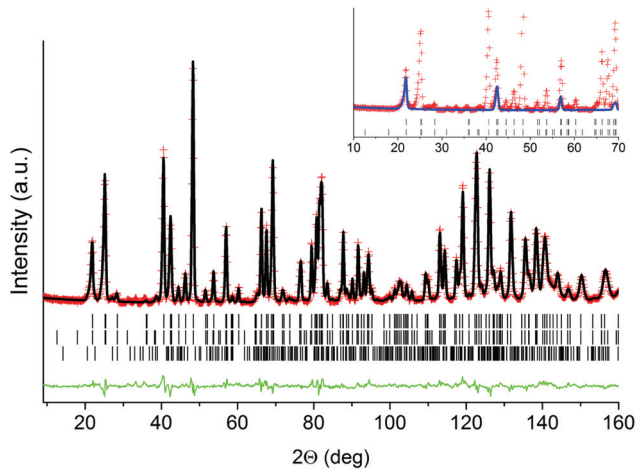

Fig. 4 Rietveld plot for the $K_2CoP_2O_7$ neutron powder diffraction data at 3 K. Red crosses and black and green solid lines indicate the observed and calculated patterns and their difference, respectively. Black tick marks indicate from top to bottom position of the nuclear and magnetic peaks of $K_2CoP_2O_7$ and peaks of KPO_3, respectively. Blue curve in the inset shows magnetic contribution. R_p = 3.81%, R_{wp} = 4.92%, χ^2 = 5.97, R_{mag} = 4.43%.

Ab initio calculations

We modelled the magnetic exchange interactions in the $K_2CoP_2O_7$ material taking into account two pathways, *i.e.* J_1 in the layer (∈ *ab*-plane) and J_2 between the layers (∉ *ab*-plane) (Fig. 5). It is expected that the interlayer interaction will be much weaker due to the absence of covalent bonds sharing electron wave functions.

$Sr_2CoGe_2O_7$ [5] crystallizes in a non-centrosymmetric melilite crystal structure with space group $P\bar{4}2_1m$ (113) while $K_2CoP_2O_7$ has a centrosymmetric twisted-melilite crystal structure. The structure of the transition metal layers in both structures is identical except that their stacking along the *c* axis is different. This difference was expected to produce only a negligible effect on magnetic interactions. However, surprisingly, NPD data showed the experimental magnetic structures of $K_2CoP_2O_7$ (this work) and $Sr_2CoGe_2O_7$ [5] to be G-type and C-type, respectively (Fig. 6a and b), *i.e.* $Sr_2CoGe_2O_7$ and $K_2CoP_2O_7$ feature antiferromagnetic planes but the interlayer coupling along the *c* axis is different, ferromagnetic and antiferromagnetic, respectively. We performed DFT calculations similar to those described for $Sr_2CoGe_2O_7$ [24] to compare the magnetic properties of these materials and evaluate the J_1 and J_2 magnetic exchange parameters.

Theory

The spin exchange magnetic interactions can be simply described by the general Heisenberg spin Hamiltonian representing a series of pair-wise spin exchange interactions (eqn (1)). This model relates the total energy of a material to its

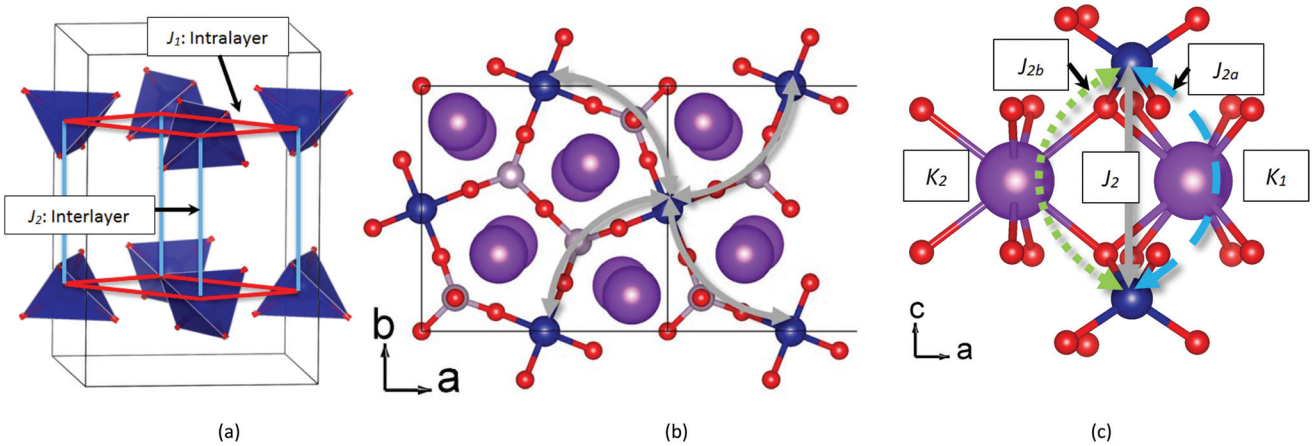

Fig. 5 (a) Overall diagram of J_1 and J_2 magnetic exchange pathways. Relationship between J_1 (b) and J_2 (c) pathways and local bond chains.

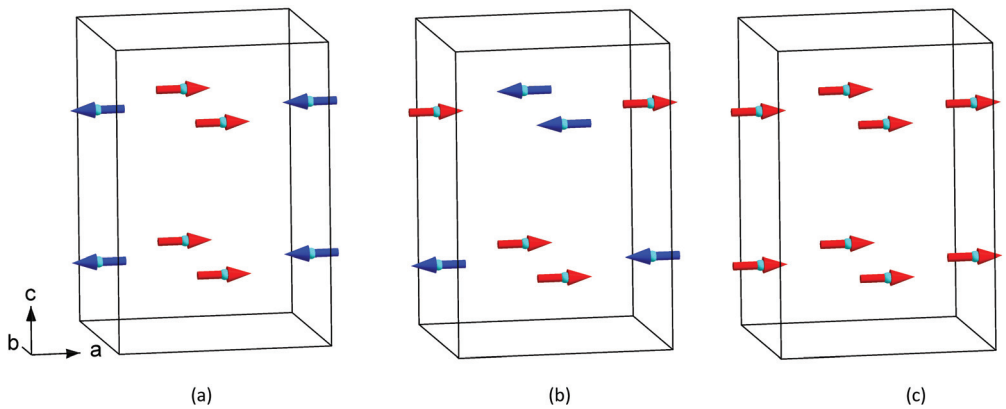

Fig. 6 Magnetic configurations used for *ab initio* calculations: C-type (a), G-type (b), ferromagnetic (c).

spin configuration and the strength of the spin-exchange interactions between neighboring magnetic sites. For our system, we model two spin exchange interactions J_1 and J_2, the intralayer and interlayer exchange interactions respectively (Fig. 5).

$$E = H_{\text{spin}} + E_{\text{non-magnetic}}; \quad H_{\text{spin}} = -\sum_{i<j} J_{ij}\hat{S}_i \cdot \hat{S}_j \qquad (1)$$

These equations can be re-arranged to express the J_i values as a function of the energy of the system in different spin configurations (eqn (2) and Fig. 6). Then, based on the spin interaction exchange constants, J_i, the Curie–Weiss temperature can be estimated in the mean field approximation (eqn (3)).

$$J_1 = \frac{4}{4 \times 3^2}(E_{\text{C-type}} - E_{\text{FM}}), \quad J_2 = \frac{4}{2 \times 3^2}(E_{\text{G-type}} - E_{\text{C-type}}) \qquad (2)$$

$$\theta = \frac{S(S+1)}{3k_{\text{B}}}\sum_i z_i J_i = \frac{15(2J_1 + J_2)}{6k_{\text{B}}} \qquad (3)$$

Geometry of exchange pathways

Examination of the bond lengths, angles and dihedral angles in the chains of bonds between the Co sites was performed to assign spin exchange constants to specific SSE pathways for $K_2CoP_2O_7$ and $Sr_2CoGe_2O_7$ (Table 2). The intralayer J_1 corresponds to the super–super exchange pathway through the Co–O–(P/Ge)–O–Co bond chain (Fig. 5b). Although another pathway which begins and ends in the same layer but passes through the adjacent K or Sr atom between the layers can be conceived, its contribution to total spin exchange should be much smaller, being highly ionic with negligible overlap integrals. Therefore, J_1 can be directly associated with the (P/Ge) SSE pathway. This type of pathway is repeated once for every J_1 pair.

The interlayer exchange parameter J_2 corresponds to the chemical Co–O–K–O–Co or Co–O–O–Co pathways, which connect the layers together (Fig. 5c). There are two symmetrically inequivalent pathways Co–O–K1–O–Co and Co–O–K2–O–Co each repeated twice (J_{2a} and J_{2b} in Table S2,† respectively). The difference between these K sites only becomes significant when considering longer diagonal spin exchange pathways between the layers. If the interlayer K atoms are not included in the pathway analysis, both pathways become symmetrically equivalent.

Table 2 Results of magnetic energy calculations for $Sr_2CoGe_2O_7$ [24] and $K_2CoP_2O_7$. Energy values are relative to those for the most stable magnetic configuration

	$Sr_2CoGe_2O_7$ [24]	$K_2CoP_2O_7$ relaxed starting from experimental twisted-melilite structure	Hypothetical melilite-type $K_2CoP_2O_7$ relaxed as C-type AFM	Hypothetical melilite-type $K_2CoP_2O_7$ relaxed as G-type AFM
Structure type	Melilite	Twisted-melilite	Melilite	Melilite
U (eV)	4.0	4.5	4.5	4.5
G-Type AFM (K FU^{-1})	0.41	0	0.012	0.016
C-Type AFM (K FU^{-1})	0	1.27	0	0
FM (K FU^{-1})	37.0	40.36	40.28	40.28
J_1 (K)	−4.11	−4.34	−4.48	−4.48
J_2 (K)	0.09	−0.28	0.0026	0.0034
θ_{DFT} (K)	−20.4	−22.4	−22.4	−22.4
θ_{exp} (K)	−18.1	−22.5	—	—

Initial ionic relaxation

Ionic relaxation was performed on $K_2CoP_2O_7$ starting with the experimental structure, G-type magnetic configuration and a U-value of 4.5 eV and the results for the relaxed structures are presented in Table S3.† The unit cell parameters were allowed to vary and the relaxations were re-started several times to eliminate the effects of Pulay stress.[25] Even though no symmetry was imposed on the degrees of freedom of the atomic positions, the final symmetry was still the same as the original symmetry space group within 10^{-5} Å.

Magnetic energies, spin exchange constants and Curie–Weiss temperature

Next, the total energy of $K_2CoP_2O_7$ of the G- and C-type antiferromagnetic, and ferromagnetic configurations (Fig. 6) were calculated using the relaxed structure and a range of U values. These energy values were used to determine the lowest energy configuration, exchange constants, and the Curie–Weiss temperature in the mean-field approximation (eqn (2) and (3); Fig. S2 and S3†). While the symmetry of the crystal structure allows both G-type and C-type magnetic configurations, the experimental configuration has the lowest energy by a significantly larger margin than the self-convergence error. Therefore these calculations correctly predict the magnetic configuration. The Curie–Weiss temperature calculated with the U value of 4.5 matches the experimental value of −22.5 K. This value is similar to values of U for Co atoms reported in the literature.[24–26] These results also show that the model is stable with changing U value. Also, the initial relaxation was repeated with U-values of 4.0 and 4.2 and the energies and spin exchange constants were evaluated for these structures. As can be seen in Fig. S2,† the value of U used during relaxation has little impact on the final calculated quantities, see ESI† for all energy values.

For comparison, the energies of the magnetic configurations, the interaction constants J_1 and J_2 and the Curie–Weiss temperature for both $K_2CoP_2O_7$ and $Sr_2CoGe_2O_7$ are also presented in Table 2. Both materials show a strong AFM intralayer interactions and a much weaker interlayer exchange. The main difference between the two materials is the sign and magnitude of the interlayer J_2 term. For $K_2CoP_2O_7$ this term is AFM and for $Sr_2CoGe_2O_7$ the term is substantially smaller and FM. The intralayer exchange in $K_2CoP_2O_7$ and $Sr_2CoGe_2O_7$ is easy to rationalize as open Co–O–O angles (141° and 140°, respectively) promote AFM coupling of d^7 Co^{2+}, in agreement with the Goodenough–Kanamori rules.[27,28] The difference in the interlayer coupling between the two materials will be explored in the following sections.

Spin orbit coupling

The effect of spin–orbit coupling was evaluated using the non-collinear spin orbit coupling setting in VASP starting with the experimental G-type magnetic configuration. An initial wide sweep of angles revealed a strong dependence of energy on moment direction out of the *ab*-plane and a weak dependence on the angle within the *ab* plane (Fig. 7). While these calculations show that the magnetic moments unambiguously prefer to lie in the *ab* plane by an energy difference of 2.38 K FU^{-1}, the dependence of energy on the angle within the *ab* plane is close to the accuracy limit of our calculations. We can speculate that magnetization measurements carried out on a single crystal might reveal that the moment can be easily re-oriented by magnetic field in the *ab* plane.

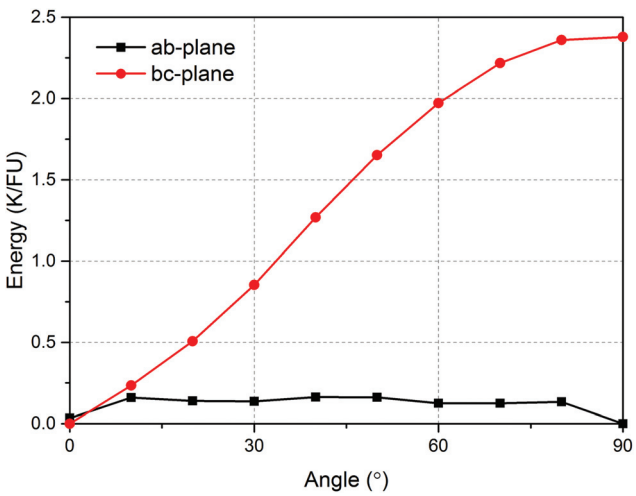

Fig. 7 Total energy as a function of out-of-plane and in-plane moment direction.

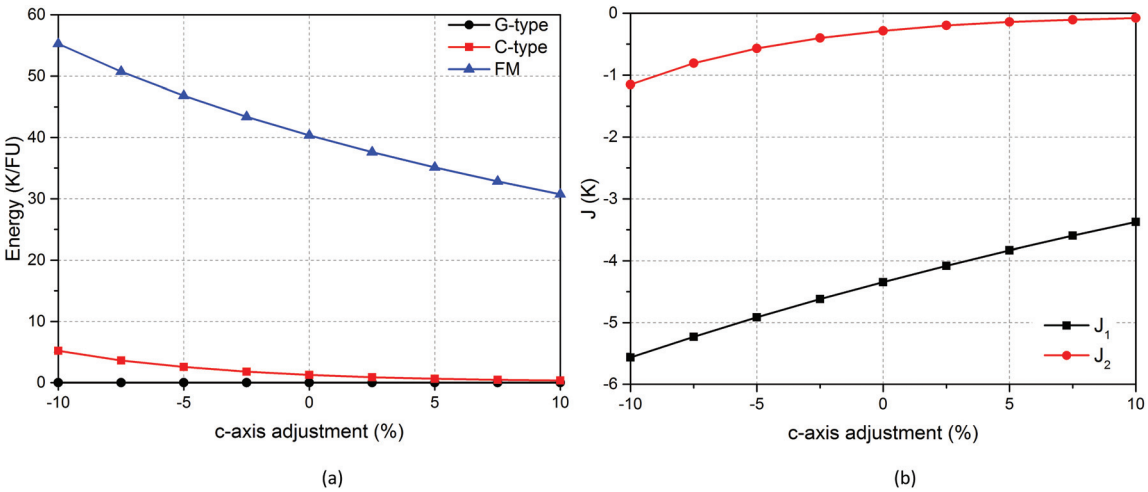

Fig. 8 (a) Total energy of considered magnetic configurations with respect to the G-type configuration taken as a baseline at E = 0; (b) exchange parameters J_1 and J_2 as a function of c-axis length relative to the relaxed value.

c-Axis compression and interlayer magnetism

The interlayer Co–Co distance in $K_2CoP_2O_7$ and $Sr_2CoGe_2O_7$ (5.58 Å and 5.31 Å, respectively) differs mainly due to the ionic radii of K^+ and Sr^{2+} (1.65 Å and 1.40 Å,[29] respectively). We therefore tried to understand whether interlayer Co–Co distance is responsible for the stabilization of the G- *vs.* C-type magnetic structure. We evaluated the effect of interlayer separation on the interlayer magnetic interactions in $K_2CoP_2O_7$ by both stretching and compressing the length of the c unit cell parameter. The energies for the magnetic configurations in (Fig. 6) and spin exchange constants were calculated with the c cell parameter adjusted over a range of ±10%, with the results shown in Fig. 8. As can be seen, adjusting the length of the c-axis did not have a dramatic effect on the ordering of the energies of the different magnetic configurations, and therefore on the magnetic ground state or the general behavior of the magnetic exchange interactions. Therefore, high-pressure experiments or chemical doping on the A site to adjust the interlayer distance are unlikely to vary the sign of the interlayer interaction. Moreover, as can be seen in Fig. 8, an increase of interlayer distance destabilizes the G-type structure with respect to the C-type and therefore the fact that $K_2CoP_2O_7$ with larger interlayer distance compared to that for $Sr_2CoGe_2O_7$ orders in as G-type cannot be explained by this factor.

Layer rotation and interlayer magnetism

To investigate whether the relative orientation of the $[CoX_2O_7]^{2-}$ layers in the melilite and twisted-melilite structure type affects the sign of the interlayer exchange parameter J_2, a hypothetical structural model of $K_2CoP_2O_7$ with the melilite structure type ($P\bar{4}2_1m$) was generated. This crystal structure was constructed by replacing Sr and Ge with K and P in the experimental melilite-type $Sr_2CoGe_2O_7$. Two separate relaxations were performed on this material, with G-type and C-type antiferromagnetic ordering, (Fig. 6) using a similar procedure to that described above. Relaxations were performed to minimize the energy differences due to structural strain, which are much larger than the energy differences due to magnetic configuration. These two magnetic configurations were selected as it is expected that the strong AFM intralayer coupling will not be significantly affected by the small geometry changes of relaxation. However, relaxation in different magnetic configurations may significantly affect the interlayer magnetic exchange as this term is much weaker.

The ionic positions of these relaxed structural models were very similar as were the final energies (Tables S4 and S5†). These relaxations show that the C-type magnetic configuration has the lowest energy by 13.4 mK FU^{-1}. Also, as expected, both magnetic configurations of the hypothetical melilite-type $K_2CoP_2O_7$ had significantly higher total energy compared to the experimental G-type twisted-melilite, by ~386 K FU^{-1}.

Next, the energies of additional magnetic configurations (Fig. 6) were calculated and the magnetic exchange pathway constants were evaluated (eqn (2) and (3); Table 2). It was found that the interlayer interaction for this new configuration is weakly ferromagnetic in contrast to the AFM interaction for the experimental twisted-melilite structure. The magnitude of the interaction between the layers is even smaller than that for $Sr_2CoGe_2O_7$. Nevertheless, these calculations suggest that it is the relative orientation of the layers that determine the sign and magnitude of the magnetic interaction between the layers. The question of whether this is a trend general for all the melilites *vs.* twisted-melilites will be investigated in subsequent experimental and computational studies.

Conclusions

The magnetic structure and properties of twisted-melilite type $K_2CoP_2O_7$ were investigated using magnetometry, neutron powder diffraction and *ab initio* calculations. This material undergoes a long-range magnetic transition into a collinear

G-type antiferromagnetic structure at 11 K, in contrast to the C-type magnetic structure of melilite-type $Sr_2CoGe_2O_7$.[5] Calculations revealed that this difference is most likely due to the different mutual orientation of $[Co(P,Ge)_2O_7]^{2-}$ layers between these two compounds, rather than the interlayer distance, which has implications for A-site doping and pressure experiments for melilite-type compounds.

The calculations for $K_2CoP_2O_7$ taking into account spin–orbit coupling also showed clear preference of Co^{2+} magnetic moments to be confined in the *ab*-plane. However, the dependence of total energy on the moment direction within the *ab*-plane is negligible suggesting the possibility of field-induced in-plane spin re-orientation transition, which could be detected by magnetometry performed on $K_2CoP_2O_7$ single crystals.

Acknowledgements

PB thanks the Department of Science and Technology, India (SR/NM/Z-07/2015) for the financial support and Jawaharlal Nehru Centre for Advanced Scientific Research (JNCASR) for managing the project.

References

1 E. Burzo, *Magnetic Properties of Non-Metallic Inorganic Compounds Based on Transition Elements: Sorosilicates, Landolt-Börnstein–Group III Condensed Matter*, 2005, p. 27.
2 J. Smith, *Am. Mineral.*, 1953, **38**, 643.
3 I. P. Swainson, M. T. Dove, W. W. Schmahl and A. Putnis, *Phys. Chem. Miner.*, 1992, **19**, 185.
4 T. Masuda, S. Kitaoka, S. Takamizawa, N. Metoki, K. Kaneko, K. Rule, K. Kiefer, H. Manaka and H. Nojiri, *Phys. Rev. B: Condens. Matter*, 2010, **81**, 100402.
5 T. Endo, Y. Doi, Y. Hinatsu and K. Ohoyama, *Inorg. Chem.*, 2012, **51**, 3572.
6 A. Zheludev, G. Shirane, Y. Sasago, N. Kiode and K. Uchinokura, *Phys. Rev. B: Condens. Matter*, 1996, **54**, 15163.
7 J. Majling, Š. Palčo, F. Hanic and J. Petrovič, *Chem. Pap.*, 1974, **28**, 294.
8 M. Gabelica-Robert, *C. R. Acad. Sci., Ser. II: Mec., Phys., Chim., Sci. Terre Univers*, 1981, **293**, 497.
9 E. Murashova, Y. A. Velikodnyj and V. Trunov, *Russ. J. Inorg. Chem.*, 1988, **33**, 904.
10 F. Sanz, C. Parada, J. M. Rojo, C. Ruiz-Valero and R. Saez-Puche, *J. Solid State Chem.*, 1999, **145**, 604.
11 A. Guesmi and A. Driss, *J. Soc. Chim. Tunis.*, 2002, **4**, 1675.
12 J. Rodríguez-Carvajal, *Phys. B*, 1993, **192**, 55.
13 G. Kresse and J. Hafner, *Phys. Rev. B: Condens. Matter*, 1994, **49**, 14251.
14 G. Kresse and J. Hafner, *Phys. Rev. B: Condens. Matter*, 1993, **47**, 558.
15 G. Kresse and J. Furthmüller, *Comput. Mater. Sci.*, 1996, **6**, 15.
16 G. Kresse and J. Furthmuller, *Phys. Rev. B: Condens. Matter*, 1996, **54**, 11169.
17 J. P. Perdew, K. Burke and M. Ernzerhof, *Phys. Rev. Lett.*, 1996, **77**, 3865.
18 P. E. Blöchl, *Phys. Rev. B: Condens. Matter*, 1994, **50**, 17953.
19 G. Kresse and D. Joubert, *Phys. Rev. B: Condens. Matter*, 1999, **59**, 1758.
20 H. J. Monkhorst and J. D. Pack, *Phys. Rev. B: Solid State*, 1976, **13**, 5188.
21 P. E. Blochl, O. Jepsen and O. K. Andersen, *Phys. Rev. B: Condens. Matter*, 1994, **49**, 16223.
22 S. Dudarev, G. Botton, S. Savrasov, C. Humphreys and A. Sutton, *Phys. Rev. B: Condens. Matter*, 1998, **57**, 1505.
23 K. Jost and H. Schulze, *Acta Crystallogr., Sect. B: Struct. Crystallogr. Cryst. Chem.*, 1969, **25**, 1110.
24 H.-J. Koo, C. Lee and M.-H. Whangbo, *J. Magn. Magn. Mater.*, 2012, **324**, 3716.
25 G. Francis and M. Payne, *J. Phys.: Condens. Matter*, 1990, **2**, 4395.
26 L. Wang, T. Maxisch and G. Ceder, *Phys. Rev. B: Condens. Matter*, 2006, **73**, 195107.
27 J. B. Goodenough, *Magnetism and the chemical bond*, Interscience Publishers, New York, 1963.
28 J. Kanamori, *J. Phys. Chem. Solids*, 1959, **10**, 87.
29 R. Shannon, *Acta Crystallogr., Sect. A: Cryst. Phys., Diffr., Theor. Gen. Cryst.*, 1976, **32**, 751.
30 M. Akaki, J. Tozawa, D. Akahoshi and H. Kuwahara, *J. Phys.: Conf. Ser.*, 2009, **150**, 042001.
31 M. Akaki, J. Tozawa, M. Hitomi, D. Akahoshi and H. Kuwahara, *J. Phys.: Conf. Ser.*, 2010, **200**, 012003.
32 M. Akaki, T. Tadokoro, H. Kuwahara, T. Kihara and M. Tokunaga, *J. Korean Phys. Soc.*, 2013, **62**, 1812.
33 B. El Bali and P. Y. Zavalij, *Acta Crystallogr., Sect. E: Struct. Rep. Online*, 2003, **59**, 59.
34 A. Zheludev, T. Sato, T. Masuda, K. Uchinokura, G. Shirane and B. Roessli, *Phys. Rev. B: Condens. Matter*, 2003, **68**, 024428.
35 T. Sato, T. Masuda and K. Uchinokura, *Phys. B*, 2003, **329**, 880.
36 H. Yi, Y. Choi, S. Lee and S.-W. Cheong, *Appl. Phys. Lett.*, 2008, **92**, 2904.
37 H. Murakawa, Y. Onose, S. Miyahara, N. Furukawa and Y. Tokura, *Phys. Rev. Lett.*, 2010, **105**, 137202.
38 I. Kézsmárki, N. Kida, H. Murakawa, S. Bordács, Y. Onose and Y. Tokura, *Phys. Rev. Lett.*, 2011, **106**, 057403.
39 V. Hutanu, A. Sazonov, M. Meven, G. Roth, A. Gukasov, H. Murakawa, Y. Tokura, D. Szaller, S. Bordács and I. Kézsmárki, *Phys. Rev. B: Condens. Matter*, 2014, **89**, 064403.
40 H. Bih, I. Saadoune and M. Mansori, *Moroc. J. Condens. Matter*, 2006, **7**, 74.
41 H. B. Yahia, R. Essehli, I. Belharouak and E. Gaudin, *Mater. Res. Bull.*, 2015, **71**, 7.

